

# PFC Simulation Study on Time-dependent Deformation Failure Properties and Energy Conversion Law of Sandstone under Different Axial Stress

Yu Wang<sup>1,2\*</sup>, Qi Liu<sup>1</sup>

<sup>1</sup> Hubei Key Laboratory of Disaster Prevention and Mitigation, China Three Gorges University, Yichang City, Hubei Province, 443002, China

<sup>2</sup> Key Laboratory of Geological Hazards on Three Gorges Reservoir Area, Ministry of Education, China Three Gorges University, Yichang City, Hubei Province, 443002, China

\* Corresponding author, e-mail: [wangyu@ctgu.edu.cn](mailto:wangyu@ctgu.edu.cn)

Received: 10 June 2022, Accepted: 06 August 2022, Published online: 18 August 2022

## Abstract

Rock burst mostly happens in deep rock engineering, which obviously performs obvious time-dependent destruction and releases huge energy. Thus, the uniaxial compressive time-dependent deformation failure tests of sandstone under different axial stress are conducted and the optimized Parallel-bonded stress corrosion (PSC) model is established based on PFC method. The results show that tension micro-cracks are the direct reason of rock bearing capacity reduction during the whole failure process. The time-dependent deformation stage is composed of the initial strain stage, the steady-state strain stage and the accelerated strain stage. As the axial stress increases, rock mass enters into the accelerated strain stage more quickly and the strain amount of time-dependent deformation stage decreases. From the comparison of energy conversion between PFC simulation and experiments, the higher elastic strain energy will be accumulated and the less dissipation energy will be produced while the axial stress increases when reaching the failure point. After the failure point, the elastic strain energy has a small increase because the strain rate changes faster than the failure relaxation rate. Based on the calculation results of residual elastic energy index ( $A_{EF}$ ), the rock burst shows a tendency that from weakness to moderation as the axial stress increases. The research results will provide a certain reference in predicting the rock burst.

## Keywords

rock burst, time-dependent, PSC model, energy conversion, residual elastic energy index

## 1 Introduction

Rock burst is a kind of geological hazard that rock mass suddenly destroys and quickly releases a large amount of energy, which mostly occurs in the hard brittle rock cave with high ground stress and no groundwater [1]. Time-dependent rock burst is extremely common in deep rock engineering [2]. In many large hydropower station constructions, such as Tianshengqiao, Taipingyi and Ertan, rock burst happens within a certain period of time after blasting and excavation [3]. Taking Jinping II hydropower station as example, the rock burst takes place after 6–15 h of excavation, showing an obvious time-dependent effect, which is mainly due to the sustainable development of rock fracture damage under high ground stress condition [4–5]. In order to clarify the time-dependent deformation failure properties of rock burst, many scholars have done a large number of studies, including laboratory test,

theoretical analysis and numerical simulation. According to the rock burst phenomenon in Jinping II Hydropower Station, Chen et al. [6] proposed that the occurrence of rock burst mainly depends on the time that the energy of the rock mass accumulates to the critical state. Especially in PFC simulation, Cui et al. [5] and Liu et al. [7] used the stress corrosion model (PSC), including the scale effect and time effect, to predict the long-term stability of the water diversion tunnel. Sun et al. [8] and Jiang et al. [9] established the numerical model of rock which can reflect its short-term and long-term strength characteristics, predicting the time-dependent deformation of rock.

Not only that, the time-dependent deformation failure is often accompanied by energy release. Energy drive is the inducement of rock failure, while rock failure is the result of accumulated damage [8]. For example, nearly a hundred

rock bursts occurred in Erlang Mountain Tunnel, which directly threatened the safety of construction works and equipment, and seriously affected the progress of the project [3]. An extremely strong rock burst occurred in the Jinping II Hydropower Station, and the total collapse amounted to more than 400 m<sup>3</sup>, which caused the permanent burial of the large equipment and many casualties of construction works [10]. In order to clarify the energy conversion mechanism of rock burst. Xie et al. [11] studied the law of energy accumulation and release based on elastic theory; Liu et al. [12] analyzed the energy evolution law by the elastic energy of each unloading point during the uniaxial graded loading and unloading process. Zhang et al. [13] and Liu et al. [14] used PFC numerical simulation to study the energy evolution law from micro-crack propagation and acoustic emission characteristics.

The research on the mechanism of rock burst mainly focused on the establishment of the time-dependent deformation failure model for prediction according to the analysis of tests and actual rock burst cases [8–10]. There are few time-dependent failure tests of rock mass, and the energy conversion mechanism of rock burst is rarely discussed from the microscopic perspective. Therefore, the uniaxial compressive time-dependent deformation failure tests were conducted, and corresponding PFC model was established by introducing optimized PSC model for a more profound understanding of the microscopic damage development, including time-dependent deformation, micro-cracks extension and failure characteristics of sandstone under different axial stress. The rationality of the model was proved by comparing with the experimental results. Then, the energy conversion law was analyzed based on the results of PFC numerical simulation and theoretical calculation. Based on this, the residual elastic energy index was cited to evaluate the rock burst tendency, which can provide some reference for relative research about energy mechanism of rock burst.

## 2 Analysis of uniaxial compressive failure test results

### 2.1 Test scheme

After excavation and unloading of underground caverns, the surrounding rock is often in a one-dimensional or two-dimensional state approximately, so it can be regarded as in the stress state of uniaxial compression [2]. Therefore, the uniaxial compressive time-dependent deformation failure test was conducted to simulate the stress state of surrounding rock. According to the reference [15], the probability of rock burst is higher when the normalized

**Table 1** Possibility of rock burst associated with normalized deviatoric stress level [15]

$(\sigma_1 - \sigma_3)/\sigma_p$	Rock mass damage	Possibility of rockburst
< 0.35	no-low	no
0.35–0.45	low	no
0.45–0.60	medium	low
0.60–0.70	medium-high	medium
> 0.70	high	high

deviatoric stress level is greater than 0.7, which is shown in Table 1. Therefore, the uniaxial compressive time-dependent failure test of sandstone was conducted under the axial stress of 0.85–0.95  $\sigma_p$ .

In this experiment, sandstone was taken from Three Gorges Reservoir Area as the test sample, which was consistent with the literature [16]. As a sericite medium grain quartz sandstone with porous calcareous cementation structure, which was composed of quartz, feldspar, debris, mica etc.al. Among them, quartz accounts for 80%, whose particle size was between 0.3–0.5 mm. The dimension of cylindrical samples was set as 50 mm × 100 mm, which followed the suggestion of the International Society for Rock Mechanics (IRSM) [17]. Macroscopically, the rock samples had a uniform particle size and good cementation with an average longitudinal wave velocity of 2200 m/s and an average density of 2600 g/m<sup>3</sup>. The prepared rock samples were conducted under different axial stress, and the test scheme was divided into two groups:

1. Uniaxial compressive failure test: The axial stress ( $\sigma_1$ ) was increased at the loading rate of 0.1 kN/s until the rock sample failed to get uniaxial compressive strength ( $\sigma_p$ ).
2. Uniaxial compressive time-dependent failure test: The axial stress ( $\sigma_1$ ) was increased at the same rate above and maintained at the planned value (0.85  $\sigma_p$ , 0.90  $\sigma_p$  and 0.95  $\sigma_p$ ), until the specimen failed.

### 2.2 Stress-strain curve and mechanical parameters

Fig. 1 shows the stress-strain curves of sandstone under different axial stress ( $\sigma_1$ ) and the basic mechanical parameters of these tests are listed in Table 2 and Table 3. As can be observed, when the axial stress ( $\sigma_1$ ) is 1.00  $\sigma_p$ , the specimen fails rapidly and the duration of damage is much shorter, and it can be regarded as a special time-dependent deformation progress. While the axial stress is 0.85–0.95  $\sigma_p$ , there is an obvious 'stable deformation expansion section' in which the axial strain continues to increase with time until the specimen fails.

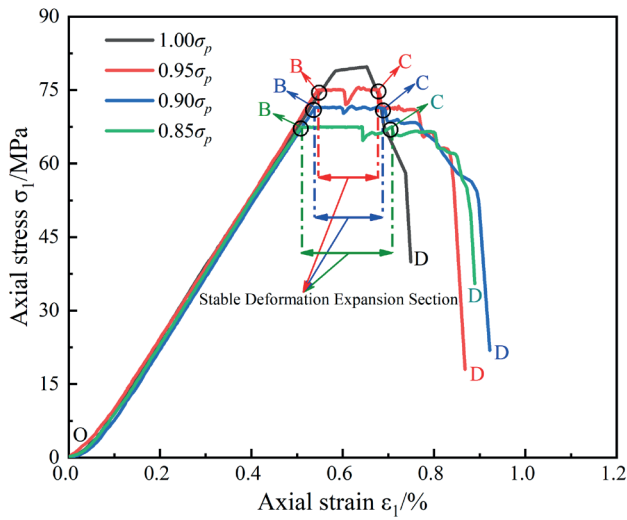


Fig. 1 Stress-strain curves under different axial stress

Table 2 Mechanical parameters of uniaxial compressive failure test

Sample	Uniaxial compressive strength $\sigma_p$ /MPa	Elastic modulus $E$ /GPa	Poisson's ratio $\mu$
1	78.76	13.00	0.23
36	79.76	13.18	0.20
Average	79.26	13.09	0.22

Table 3 Mechanical parameters of uniaxial compressive time-dependent deformation failure test

Sample	Axial stress $\sigma_1$ /MPa	Elastic modulus $E$ /GPa	Poisson's ratio $\mu$
2	0.95 $\sigma_p$ (75.53)	13.24	0.23
3	0.90 $\sigma_p$ (73.67)	12.35	0.20
4	0.85 $\sigma_p$ (67.50)	12.75	0.21

The method for determining the failure point C is through the variation law of volumetric strain. Taking the axial stress of  $0.95 \sigma_p$  as example, which is shown in Fig. 2. When reaching the point B, the stress-strain curve appears to fluctuate and the volume strain drops slightly. After the point C, the stress-strain curve shows a significant step-down, but the volumetric strain shows an obvious turning point and decreases significantly. Therefore, the failure point C can be determined by the turning point of volumetric strain. In summary, when the axial stress ( $\sigma_1$ ) is  $0.85\text{--}1.00 \sigma_p$ , it can be seen as follows by analyzing the characteristics of the curve:

1. In the initial compaction stage and the elastic stage (OB), the stress-strain curves of different axial stress ( $\sigma_1$ ) are basically coincident, indicating that the selected specimens have less discreteness. In the

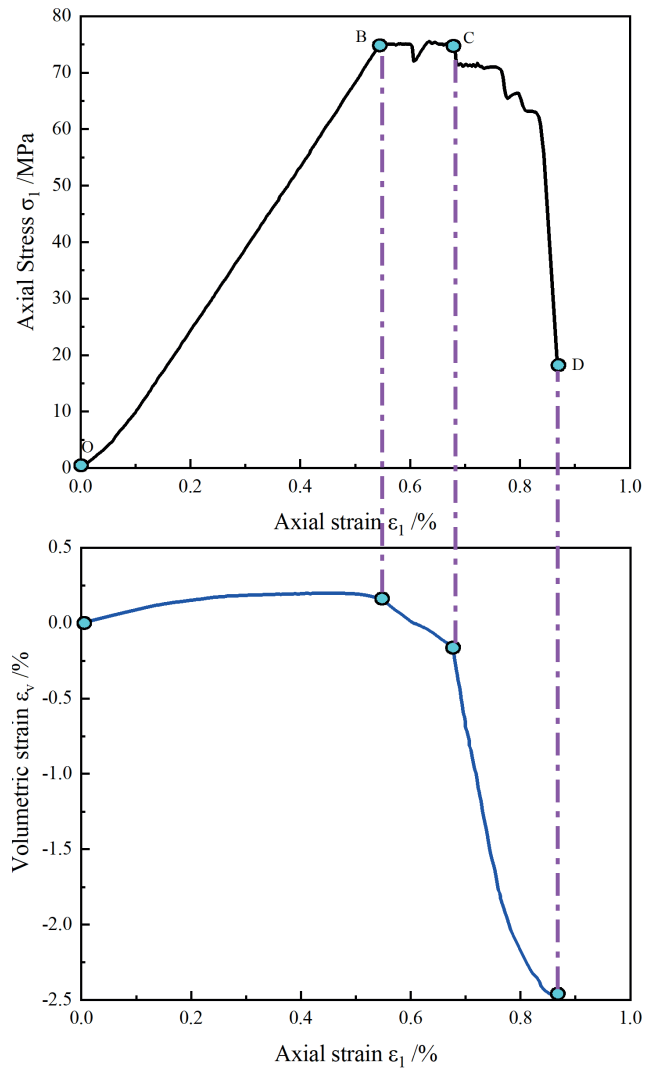


Fig. 2 Determination of failure point C ( $\sigma_1 = 0.95 \sigma_p$ )

time-dependent deformation stage (BC), the axial strain at the failure point (C) decreases with the axial stress ( $\sigma_1$ ) increases, which means that the rock mass undergone too much damage under the lower axial stress and cost longer time.

2. In the time-dependent deformation stage (BC), when the stress exceeds the long-term strength of the rock mass, the damage will continue to develop even if the axial stress is maintained at a stable constant value [2]. Due to the stress concentration effect, when the accumulation reaches the critical value, the rock mass will generate serious deformation and failure in a short time. Moreover, the curves show a significant drop after failure point (C), which means the transformation from the time-dependent deformation stage to the failure stage.

### 3 PFC Simulation of the uniaxial compressive time-dependent deformation failure test

#### 3.1 Establishment of PFC numerical model

Particle Flow Code is a discrete element program, which is commonly used to simulate the macroscopic mechanical response of materials by the bonded properties of the particles inside the grains and at the grain boundaries. In the existing bonding models, the contact-bonded model (CBM) and parallel-bonded model (PBM) are the most classical [18]. In view of PBM transferring interparticle contact bending moments besides contact forces [19–21], it is chosen to simulate sandstone, which is composed of mineral particles and interparticle cement, to make the calculation results closer to the real situation.

Firstly, the wall of rectangular geometric model is established, whose dimension is set as 50 mm × 100 mm. Secondly, considering the failure mode of rock samples, the particle radius should be set to less than 0.60 mm [22], and the particle radius ratio of maximum-minimum particle is 1.66, which conforms to the basic properties of the rock sample [18]. Therefore, combined with actual particle size of sandstone, the particle radius of model is set to 0.3–0.5 mm. Thirdly, the particles are generated with large overlap in the wall- enclosed area and make the particle system uniform by the servo mechanism. Finally, the contact is added to the particles and clear the model state (including particle velocity, displacement, etc.). The built numerical model is shown in Fig. 3.

#### 3.2 Parameters calibration

At present, a great number of numerical investigations have been conducted to study the calibration between macro-parameters and micro-parameters in details [23] and the macro-parameters of the model are affected by multiple micro-parameters. To ensure that the macroscopic mechanical response of PFC simulation is consistent with experiments under uniaxial compressive test, the micro-parameters of Table 4 are calibrated so that the basic mechanical parameters ( $\sigma_p, E, \mu$ ) of sandstone corresponding to the numerical simulation calculation results. When selecting the optimal micro-parameters, the *trial and error* method is adapted to adjust a certain parameter continuously in each numerical simulation test until the macro-parameters ( $\sigma_p, E, \mu$ ) are consistent with experiments. The calibration process is as follows:

In the whole process, the ratio of  $E_c$  and  $\bar{E}_c$  is set to 1.0, the particle stiffness ratio ( $K_n/K_s$ ) and the PBM stiffness ratio ( $\bar{K}_n/\bar{K}_s$ ) are set to the same. Firstly, the micro elastic

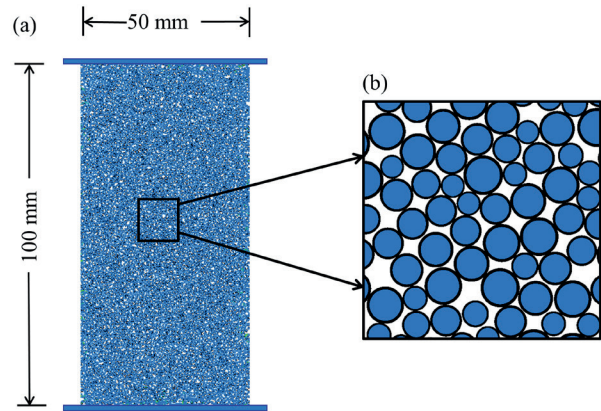


Fig. 3 PFC model of rock sample: (a) whole model of sample, (b) local model of sample

Table 4 Microscopic mechanical parameters

Parameter type	Microscopic parameters	Value
Basic particle parameters	Particle density $\rho/\text{Kg}\cdot\text{m}^{-3}$	2600
	Particle radius ratio $R_{\max}/R_{\min}$	1.66
	Particle minimum radius $R_{\min}/\text{mm}$	0.3
	Particle elastic modulus $E_c/\text{GPa}$	10.5
	Particle stiffness ratio $K_n/K_s$	1.3
	Particle friction coefficient $\mu$	0.5
	PBM contribution factor $\bar{\lambda}$	1.0
PBM parameters	PBM elastic modulus $\bar{E}_c/\text{GPa}$	10.5
	PBM stiffness ratio $\bar{K}_n/\bar{K}_s$	1.3
	PBM tensile strength $\bar{\sigma}_c/\text{MPa}$	64
	PBM cohesion strength $\bar{C}/\text{MPa}$	71
	PBM friction angle $\phi/^\circ$	32

Notes:  $R_{\max}$  is the maximum radius of particles,  $K_n$  is the particle normal stiffness,  $K_s$  is the particle tangential stiffness.  $\bar{K}_n$  is the PBM normal stiffness,  $\bar{K}_s$  is the PBM tangential stiffness

modulus (including  $E_c$  and  $\bar{E}_c$ ) are calibrated, which have certain algebraic relationships with the macro elastic modulus  $E$ . The  $E_c$  increases with  $E$  increases. By adjusting the values of  $E_c$  constantly in each numerical experiment until the result of mechanical parameters ( $E$ ) is suitable, then determine the value of  $E_c$  and  $\bar{E}_c$ . Then Poisson's ratio ( $\mu$ ) and peak strength ( $\sigma_p$ ) are calibrated and the calibration process is similar. It should be noted that the particle stiffness ratio ( $K_n/K_s$ ) mainly affects the Poisson's ratio  $\mu$ . As the stiffness ratio ( $K_n/K_s$ ) is increased, the  $\mu$  also increases. There is a polynomial relationship between PBM tensile strength  $\bar{\sigma}_c$  and the peak strength  $\sigma_p$ . The  $\sigma_p$  increases with  $\bar{\sigma}_c$  increases. The ratio between PBM tensile strength ( $\bar{\sigma}_c$ ) and PBM cohesion strength ( $\bar{C}$ ) of particles is the main reason which affects the failure mode of rock samples. And with the increase of the ratio, the failure mode shows

a transition from tensile failure to shear failure. After a series of sensitivity analysis, the calibrated parameters are listed in the Table 4.

### 3.3 Macro-micro parameters and failure mode comparison

In order to prove the rationality of the calibrated microscopic parameters, the simulation calculation and test results are compared under the axial stress of  $1.00 \sigma_p$ . Fig. 4 shows that numerical results are in good agreement with experiments discussed previously. In terms of failure mode, the main crack is caused by tensile failure inside the rock at the upper and lower ends, which reflects the tensile failure characteristics of sandstone under uniaxial compression condition.

### 3.4 Optimized PSC model

#### 3.4.1 PSC model principle

According to the fracture mechanics, a micro-crack initiation threshold ( $\sigma_a$ ) exists during the fracture propagation process [24]. When the axial stress ( $\sigma_1$ ) is more than this threshold, the micro-cracks will continue to initiate, propagate and coalesce, until they form macro-cracks, resulting in the specimen failure. This phenomenon of rock mass persistent deterioration under constant axial stress is defined as the stress corrosion. In order to truly simulate the stress corrosion process, the stress corrosion model (PSC) [25] is put forward and shown in Fig. 5. Where the microscopic aging damage degree of rock mass is represented by continuing to reduce the bonding radius  $\bar{R}$  of PBM, which can be expressed as follows (Eq. (1)):

$$\bar{R} = \begin{cases} \bar{R}_0 & (\sigma < \sigma_a) \\ \bar{R}_0 - \beta_1 e^{\beta_2 \left(\frac{\sigma}{\sigma_c}\right) t} & (\sigma_a \leq \sigma < \sigma_c) \\ 0 & (\sigma > \sigma_c) \end{cases}, \quad (1)$$

where  $\bar{R}_0$  and  $\bar{R}$  is the bonding radius of PBM before and after the stress corrosion,  $t$  is the stress corrosion time,  $\beta_1$ ,  $\beta_2$  are the constants of rock mass, which only vary with the temperature and chemical environments.  $\sigma_a$  is the micro-crack initiation threshold of PBM,  $\sigma_c$  is the normal tensile strength of PBM.

According to Eq. (1), when  $\sigma_a < \sigma < \sigma_c$ , the bonding radius  $\bar{R}$  will decrease exponentially, which means the normal tensile force, the tangential shear force and bending moments on PBM will be updated. In addition, the bonding radius

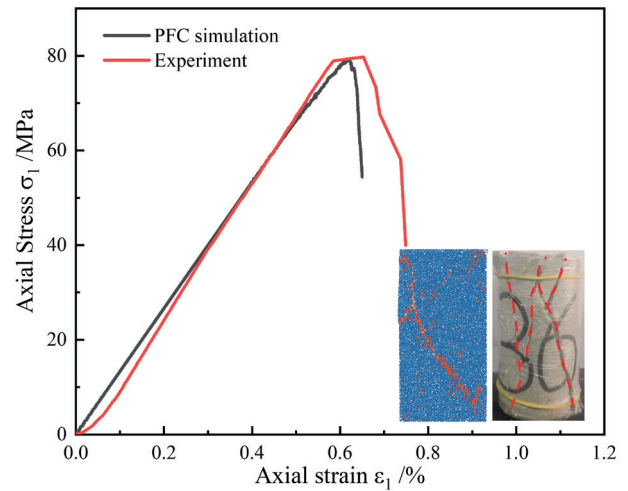


Fig. 4 Stress-strain curves of uniaxial compression test and PFC simulation

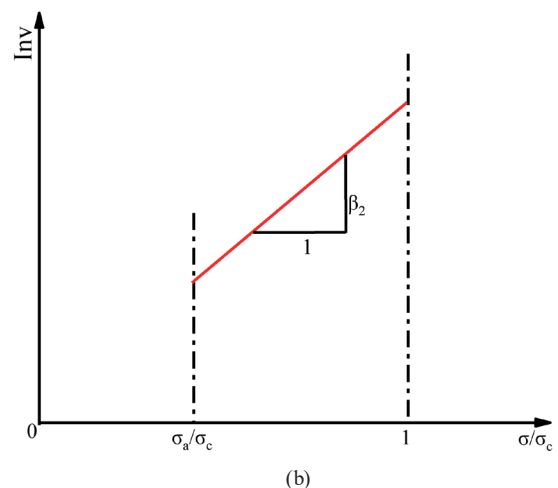
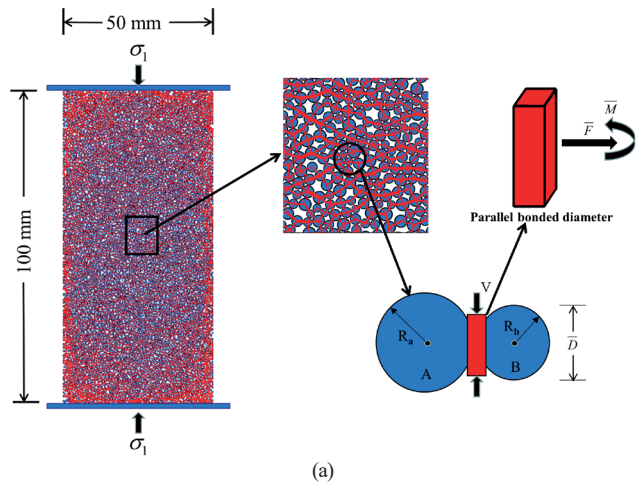


Fig. 5 Schematic of PSC model: (a) micro schematic diagram of PSC model, (b) stress corrosion rate curve

$\bar{R}$  of PBM between particles will not change when  $\sigma < \sigma_a$ , and the bonding radius  $\bar{R}$  of PBM will disappear instantaneously when  $\sigma > \sigma_c$ .

Generally speaking, the PSC model starts from the result of rock strength attenuation, and the stress state is regarded as a controlling parameter to simulate internal micro-cracks propagation. Moreover, Manouchehrian and Cai [26] and Wu et al. [27] found that the development and propagation of micro-cracks not only lead to rock strength deterioration, but also a decrease of rock stiffness. As the internal damage of the rock sample increases, micro-cracks propagate to form macroscopic cracks, resulting in reducing rock strength and stiffness. At the meantime, the particle normal stiffness mainly influences the macroscopic elastic modulus, which is the scale of describing the resistance to elastic deformation of rock mass [24]. Therefore, the rock stiffness attenuation also reflects the process of the rock mass elastic deformation ability reduction. In order to better simulate the variation law of rock mass deformation with time, the particle normal stiffness is considered to reflect the deformation characteristics of the rock mass with time, and the law of stiffness change is as follows (Eq. (2)):

$$G = \begin{cases} G_0 & (\sigma < \sigma_a) \\ G_0 - \alpha_1 t & (\sigma_a \leq \sigma < \sigma_c) \\ 0 & (\sigma > \sigma_c) \end{cases}, \quad (2)$$

where  $G_0$  and  $G$  is the particle normal stiffness before and after the stress corrosion,  $\alpha_1$  is the constants of materials. The detailed implementation procedure is as follows:

1. The axial stress is loaded to the planned value ( $0.85 \sigma_p$ ,  $0.90 \sigma_p$ ,  $0.95 \sigma_p$ ) with a certain loading rate respectively, then keep the particle system balanced by the servo system of PFC.
2. The PSC model is activated and the axial stress ( $\sigma_1$ ) is maintained at the planned value by the servo system of PFC. At the same time, the data (including test time, strain, the number of micro-cracks, etc.) can be obtained.
3. The test is completed when one of the following two conditions is satisfied: (1) The mechanical calculation in each time step is not balanced, which corresponds to the phenomenon that the specimen has undergone too much damage and cannot continue to bear load. (2) The axial strain reaches a certain value, which corresponds to the large enough deformation of the sample.

### 3.4.2 Numerical calculation process based on PSC model

The *trial and error* method is adapted in our study, and the calibration results of PSC microscopic mechanical parameters are based on the failure time ( $t_f$ ) during the time-dependent deformation stage. Obviously, the main control parameters of the PSC model are  $\alpha_1$ ,  $\beta_1$ ,  $\beta_2$ ,  $\sigma_a$  in Eqs. (1) and (2). Fig. 6 shows parameter sensitivity analysis of  $\alpha_1$ ,  $\beta_1$ ,  $\beta_2$  and  $\sigma_a$  under the axial stress of  $0.95 \sigma_p$ . Firstly,  $\beta_1$  and  $\beta_2$  are adjusted to ensure that  $t_f$  is in the range of  $10^2$ – $10^3$  s.

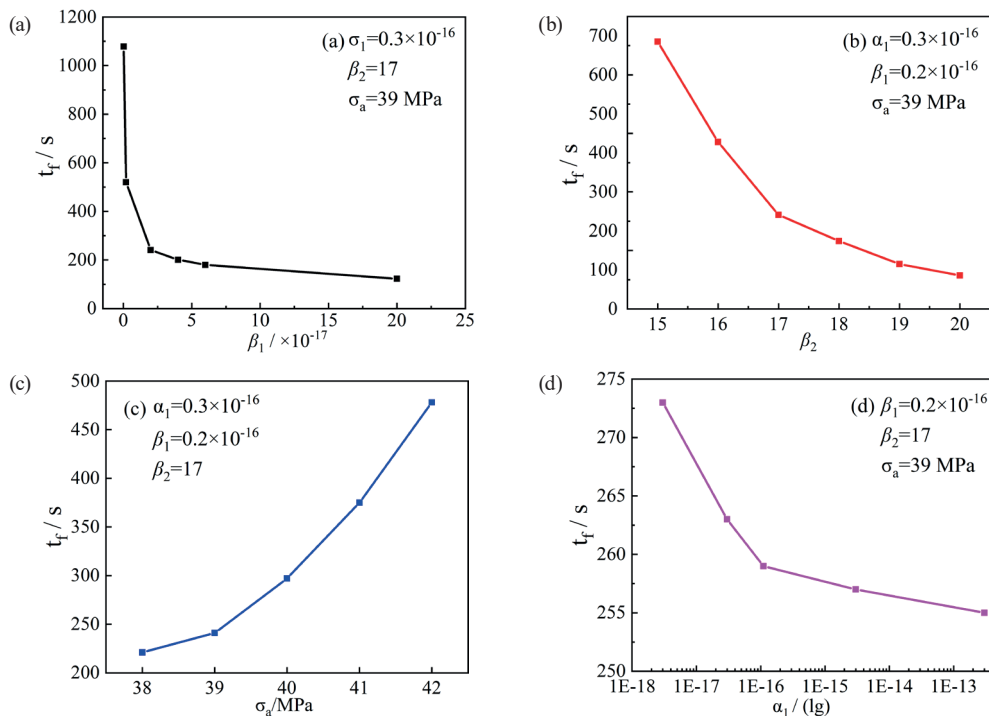


**Fig. 6** Sensitivity analysis of microscopic mechanical parameters: (a) the variation of  $t_f$  with  $\beta_1$ , (b) the variation of  $t_f$  with  $\beta_2$ , (c) the variation of  $t_f$  with  $\sigma_a$  and (d) the variation of  $t_f$  with  $\alpha_1$

Then,  $\sigma_a$  and  $\alpha_1$  are adjusted until  $t_f$  obtained by numerical test is consistent with the laboratory test basically. The calibrated results are shown in Table 5.

### 3.4.3 Comparative analysis of PFC simulation and experimental results

Fig. 7 shows the comparative results of stress-strain curves under different axial stress, and it is found that the curve variation law of PFC model calculation is basically consistent with tests during the whole process. The stress drop point (Point C and C' in Fig. 7) is defined as the failure point of the sample, and the time-dependent deformation stage is from point B (B') to point C (C'). It can be seen from the Table 6 that the axial strain is basically between 0.62% and 0.66% at point C in the PFC model, and with the axial stress decreases, the strain amount increases during BC stage, which is consistent with the experimental results. Therefore, the PSC model can well capture the time-dependent deformation characteristics.

## 4 Research on energy conversion and failure mode

### 4.1 Energy conversion analysis of PFC simulation

During the process of PFC numerical simulation calculation, the energy is obtained such as boundary energy, elastic strain energy, friction energy and dissipated energy. Specifically, the accumulated elastic strain energy ( $U^e$ ) is composed of the particle strain energy and the parallel bond strain energy, and the boundary energy ( $U$ ) is the total input energy of the system. The  $U^f$  is a part of  $U^d$ , which has the same law with  $U^d$ . and the friction energy ( $U^f$ ) is related to the generation of micro-cracks and sliding displacement of particle, which is expressed as:

$$U^f = \sum_{N_c} \left( \overline{F_i^S} (\Delta U_i^s)^{slip} \right), \quad (3)$$

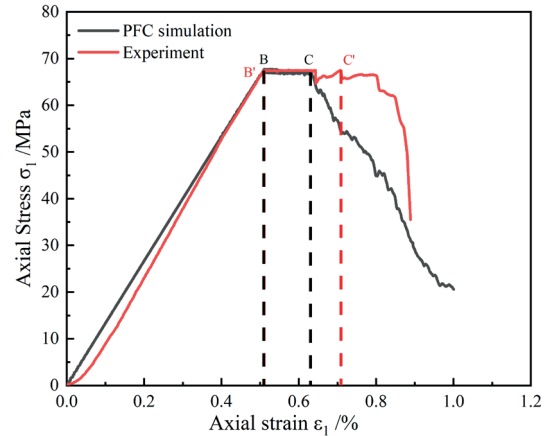
where  $N_c$  is the total number of contacts,  $\overline{F_i^S}$  is the average shear force between particles,  $(\Delta U_i^s)^{slip}$  is the sliding displacement increments of particles.

The stress-strain curve can be divided into four stages combined with the energy conversion (shown in Fig. 8).

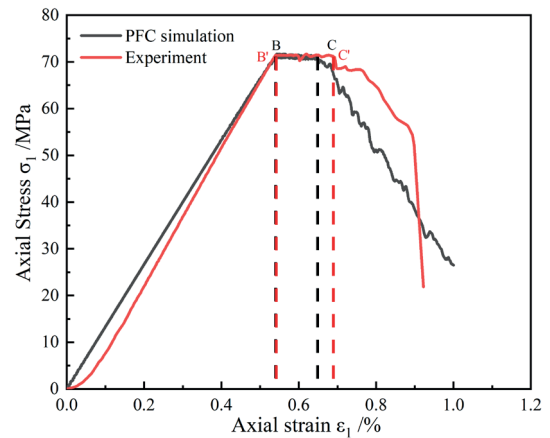
1. Initial compaction stage (OA): Because no micro-cracks appear during this stage, so the energy input is almost all converted to  $U^e$ ,  $U^d$  and the  $U^f$  are 0 basically.

Table 5 Microscopic mechanical parameters of PSC model

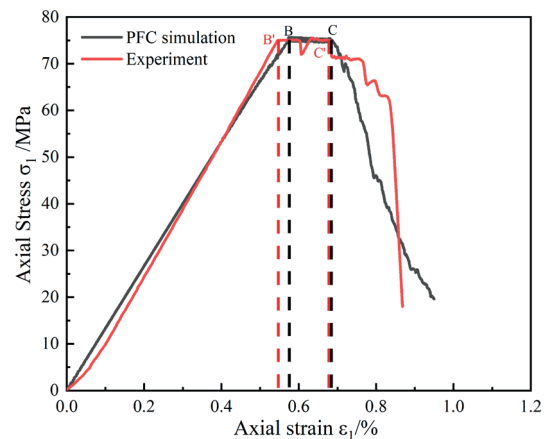
$\alpha_1$	$\beta_1$	$\beta_2$	$\sigma_a$ /MPa	$\sigma_c$ /MPa
$0.3 \times 10^{-16}$	$0.2 \times 10^{-16}$	17	39	64



(a)



(b)



(c)

Fig. 7 Comparison of stress-strain curves between test results and PFC simulation: (a)  $0.85 \sigma_p$ , (b)  $0.90 \sigma_p$  and (c)  $0.95 \sigma_p$

Table 6 Strain of point B(B') and C(C')

Axial stress / MPa	$0.85 \sigma_p$	$0.90 \sigma_p$	$0.95 \sigma_p$
Strain of point B(B')/%	0.509 (0.510)	0.541 (0.539)	0.573 (0.545)
Strain of point C(C')/%	0.622 (0.706)	0.642 (0.681)	0.656 (0.679)

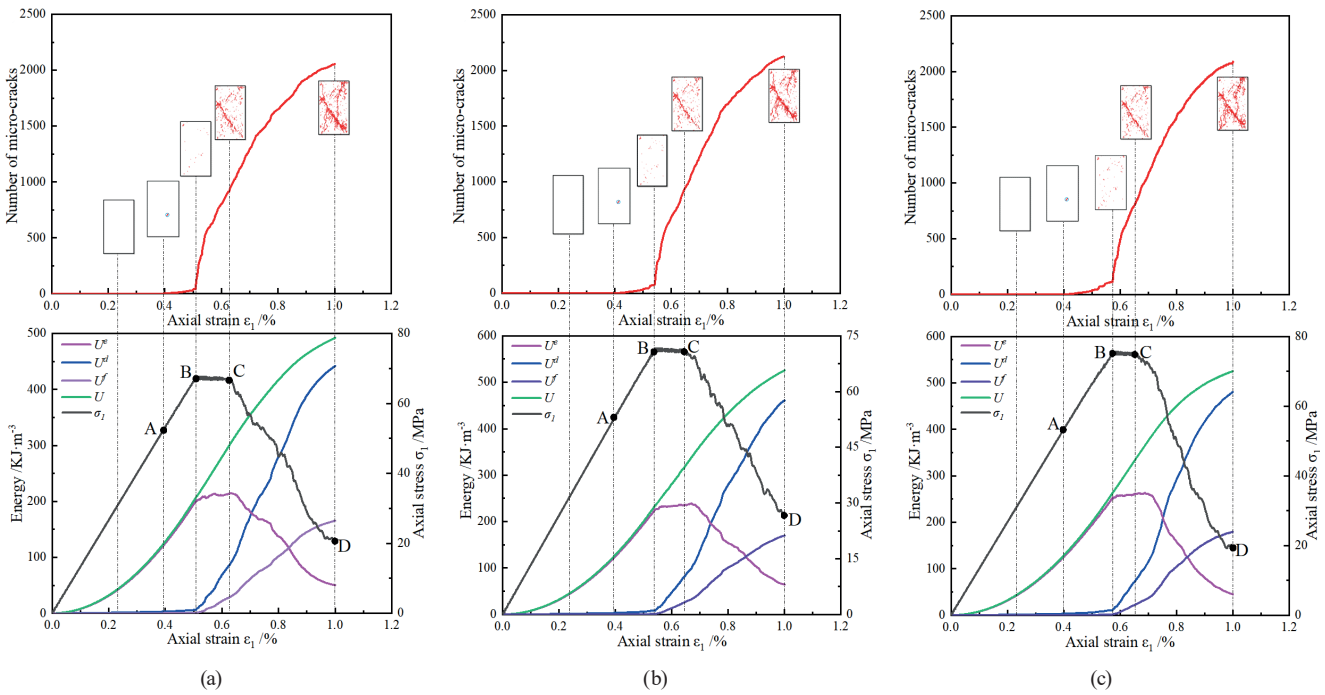


Fig. 8 Variation law of energy and micro-cracks with stress-strain: (a) 0.85  $\sigma_p$ , (b) 0.90  $\sigma_p$  and (c) 0.95  $\sigma_p$

2. Linear elastic and initial micro-crack development stage (AB): The micro-cracks began to grow slowly after point A as the input energy increases, which shows the bonds between particles started to break. And the initiation of micro-cracks extends at a small rate, which causes the slow increase of  $U^f$  and  $U^d$ .
3. Time-dependent deformation stage (BC): The micro-cracks unstably propagate under the constant axial stress ( $\sigma_1$ ), resulting in the growth rate of particle friction energy and particle surface dissipation energy increasing quickly. Therefore, the  $U^f$  and  $U^d$  increase rapidly.
4. Failure stage (CD): As the micro-cracks continue to expand until the rock mass finally fails, the  $U^e$  begins to decrease with the continuous increase of  $U^f$  and  $U^d$ .

## 4.2 Micro-crack propagation and failure mode analysis

### 4.2.1 Micro-crack propagation characteristics

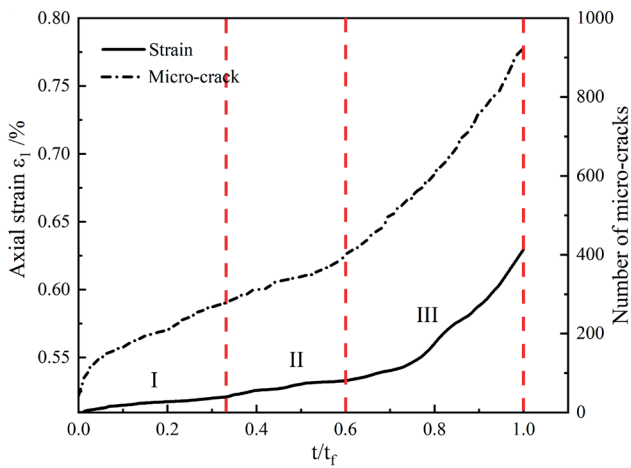
The essence of macroscopic fracture is the continuous development of internal microscopic damage. It is obvious from Fig. 8 that the micro-cracks propagate rapidly in the time-dependent deformation stage (BC). In order to clarify the inherent law and essential characteristics of time-dependent failure, the micro-crack development and strain variation of BC stage are studied, which is shown in Fig. 9.

Table 7 lists the micro-crack number of failure point C and the duration of BC stage, it is found that the number of micro-cracks decreases as the axial stress ( $\sigma_1$ )

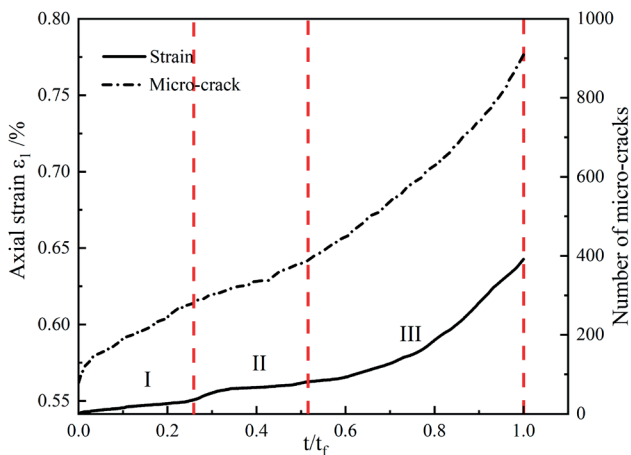
increases, which means the development of micro-cracks is insufficient during shorter time under higher axial stress ( $\sigma_1$ ). In addition, noted that in Fig. 9, the variation law of the number of micro-cracks with time is basically the same as the law of axial strain, which reflects the characteristics of the three stages: the initial strain stage, the steady-state strain stage and the accelerated strain stage. Moreover, the initial strain stage becomes shorter and the specimen enters the accelerated strain stage rapidly as the axial stress ( $\sigma_1$ ) increases.

### 4.2.2 Failure mode

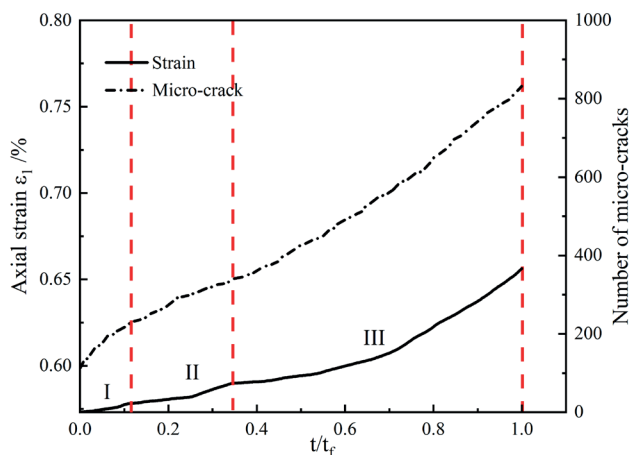
In order to deeply understand the time-dependent deformation failure characteristic of rock mass, some representative images were chosen to illustrate the features of rock fracture during BC stage of 0.85  $\sigma_p$ , as shown in Fig. 10. At the beginning of loading (Figs. 10(a)–(c)), the tensile micro-cracks are dominant, which have a relatively scattered spatial distribution. As time goes on (Figs. 10(d)–(e)), a large number of micro-cracks appear, and the generation of shear micro-cracks is characterized by local damage concentration. Subsequently, a rapid increase in damage leads to the reduction of rock bearing capacity during the stage of micro-crack accelerated propagation, and the macroscopic failure surfaces are formed finally (Fig. 10(f)). In terms of the failure form of rock mass, the tensile micro-cracks are always dominant, and only a small amount of shear micro-cracks initiate during the whole failure



(a)



(b)

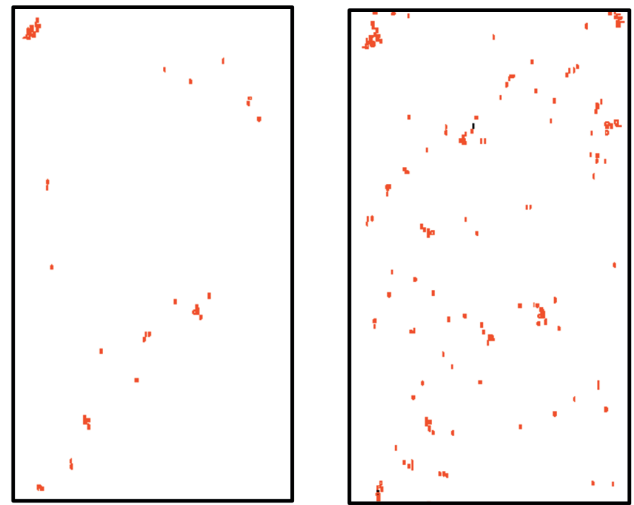


(c)

Fig. 9 Variation law of axial strain and micro-cracks with time:  
 (a)  $0.85 \sigma_p$ , (b)  $0.90 \sigma_p$  and (c)  $0.95 \sigma_p$

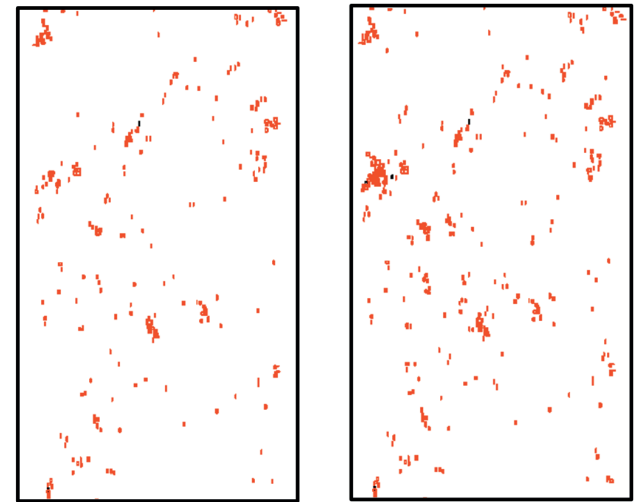
Table 7 Micro-crack number at failure point C and duration of BC stage

Axial stress $\sigma_1$ /MPa	$0.85 \sigma_p$	$0.90 \sigma_p$	$0.95 \sigma_p$
Micro-cracks number at failure point C/ $c^*$	932	909	832
Duration of BC stage $t/s$	1002	532	241



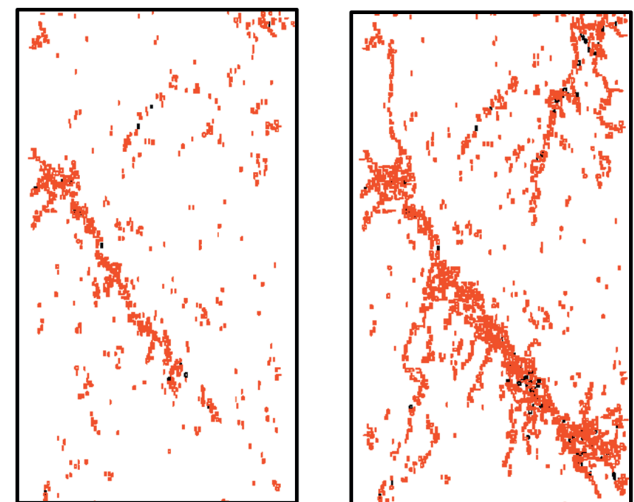
(a)

(b)



(c)

(d)



(e)

(f)

Fig. 10 Micro-cracks distribution during BC stage under  $0.85 \sigma_p$ :  
 (a) 0 s, (b) 51 s, (c) 200 s, (d) 449 s, (e) 799 s, (f) 1007 s

process, which is far less than the tensile micro-cracks (black: shear micro-cracks, red: tensile micro-cracks), it is consistent with the failure mode of rock mass under uniaxial compression test [28].

**4.3 Comparison of energy conversion between theoretical calculation and PFC simulation calculation.**

Based on the energy theory, the failure process of rock mass is accompanied by the energy dissipation and energy release during the uniaxial compression test. Xie et al. [29] assumed that rock mass did not exchange heat with the outside world under outer force. According to the first law of thermodynamics:

$$U = U^d + U^e, \tag{4}$$

where  $U$  is the total input work,  $U^d$  is the dissipation energy,  $U^e$  is the elastic strain energy.

Fig. 11 shows the corresponding relationship between the  $U^d$  and  $U^e$  (shadow area) in the stress-strain curve, in which  $E_u$  is the unloading modulus.

In the uniaxial compression test, the elastic strain energy  $U^e$  is [29]:

$$U^e = \frac{\sigma_1^2}{2\bar{E}}, \tag{5}$$

where  $\bar{E}$  is the elastic modulus, which replaces the  $E_u$  [30];  $\sigma_1$  is the axial stress.

Fig. 12 shows that the energy conversion law of PFC simulation is consistent with the theoretical calculation results of  $U^e$ , which is obtained according to Eq. (5) based on the experimental date. But it should be noted that the change trend of  $U^e$  is obviously different during the BC stage. In the numerical simulation, most of the input

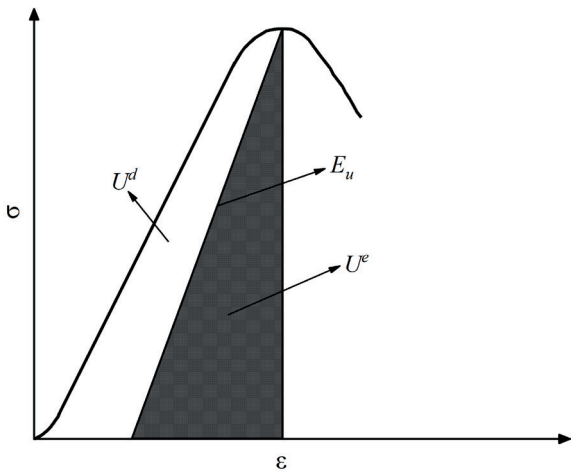


Fig. 11 Corresponding relationship between elastic strain energy and dissipated energy

energy is dissipated, which is converted into the surface energy of micro-cracks propagation and a small part is converted into  $U^e$ .

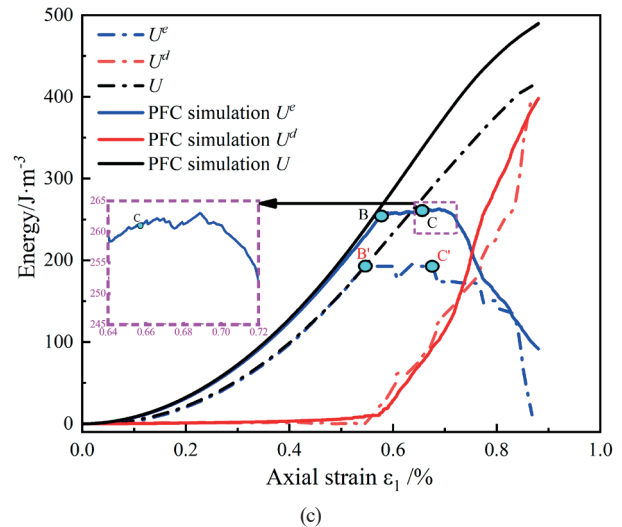
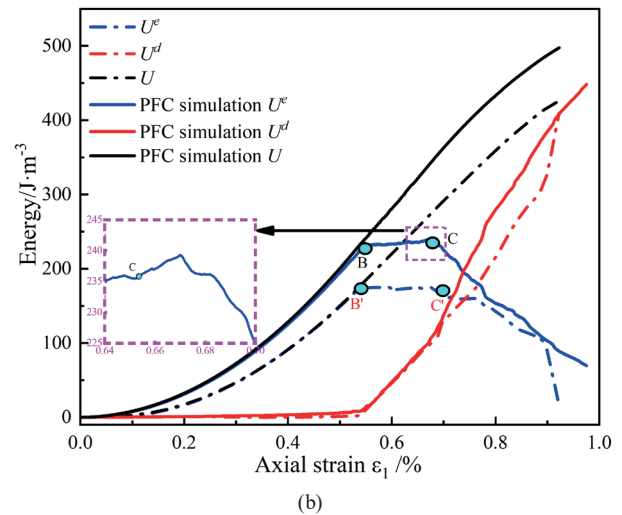
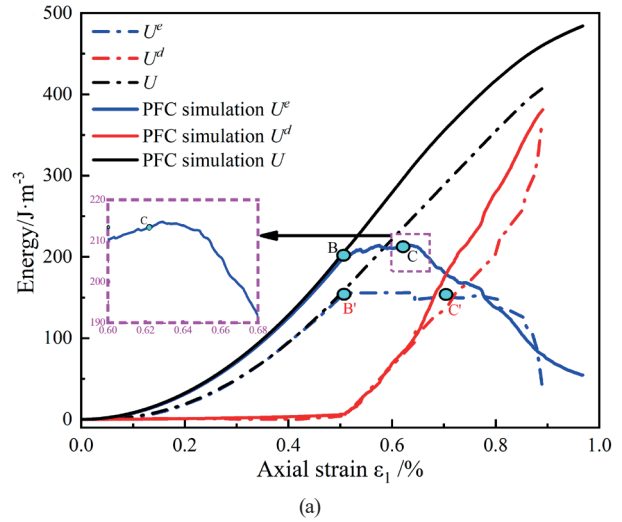


Fig. 12 Energy comparison curves between theoretical calculation and PFC simulation calculation: (a)  $0.85 \sigma_p$ , (b)  $0.90 \sigma_p$  and (c)  $0.95 \sigma_p$

In addition, we can see that there is a small increase in strain energy after point C (partial enlarged detail in Fig. 12). This is mainly because the strain rate changes faster than the failure relaxation rate when the rock mass fails, that is to say, rock mass will continue to absorb input energy and release  $U^d$  at the same time. Therefore, it is rational to analyze the energy conversion law by the method of PFC numerical simulation. Finally, the energy conversion results of failure point C are shown in Table 8, it can observe that:

1. The absorbed  $U^e$  increases while the axial stress ( $\sigma_1$ ) increases, which accounts for more than 70.8% of the input energy  $U$ . The required  $U^d$  decreases during the failure process of rock mass, that is to say, the more energy is absorbed as the axial stress ( $\sigma_1$ ) increases when the rock mass fails.
2. As the axial stress ( $\sigma_1$ ) increases, the internal micro-cracks will not develop fully when the rock mass fails quickly. The  $U^f$  accounts for 6.9–9.7% of the  $U$  under the axial stress of 0.85–0.95  $\sigma_p$ . When the axial stress of is 1.00  $\sigma_p$ , the  $U^f$  is much smaller than other axial stress, because the generated micro-cracks decrease and the sliding displacement of particles also decreases.

Fig. 13 is the curve of energy at failure point C under different axial stress ( $\sigma_1$ ). It can be seen that  $U^e$  has an obvious linear relationship, and  $U^d$  and  $U^f$  show a consistent variation law, the  $U^f$  accounts for 30.6–33.3% of the  $U^d$  under the axial stress of 0.85–0.95  $\sigma_p$ , but  $U^d$  and  $U^f$  decreases significantly under the axial stress of 1.00  $\sigma_p$ , which accounts for 20.9%. Because the rock mass fails rapidly and the duration of destruction is much shorter, resulting in the micro-cracks incomplete extension. Therefore, the  $U^d$  and  $U^f$  under the axial stress of 1.00  $\sigma_p$  is much lesser than other axial stress.

Through the above analysis, it can find that  $U^e$  is mainly used to store internal energy before failure point C, and the stored  $U^e$  are mainly converted into  $U^d$  after failure point C, which is mainly used for the generation and further

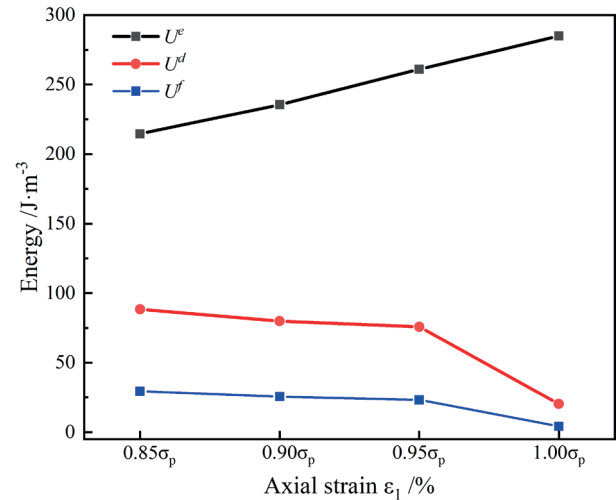


Fig. 13 Energy curves under different axial stress

development of micro-cracks, resulting in the attenuation of rock strength and the generation of macro-cracks. The rock mass will destroy until it exceeds the storage limit.

#### 4.4 Judgement of rock burst tendency

The energy emitted by rock burst mainly comes from the residual elastic energy of rock mass after overall failure, which reflects the characteristics of rock burst tendency. Therefore, the residual elastic energy index ( $A_{EF}$ ) is used to measure rock burst tendency [31], and the formula is as follows:

$$A_{EF} = U^e - U^a, \tag{6}$$

where the  $U^e$  is the elastic strain energy before the rock fails,  $U^a$  is the failure energy after the rock mass fails.

Fig. 14 shows the corresponding relationship between the  $U^e$  and  $U^a$ , and the rockburst tendency can be divided into four grades according to the value of AEF, which is as follows:

$$\begin{cases} \text{No rockburst} : A_{EF} < 50 \text{kJ} \cdot \text{m}^{-3} \\ \text{Weak rockburst} : A_{EF} = 50 \sim 150 \text{kJ} \cdot \text{m}^{-3} \\ \text{Moderate rockburst} : A_{EF} = 150 \sim 200 \text{kJ} \cdot \text{m}^{-3} \\ \text{Intense rockburst} : A_{EF} > 200 \text{kJ} \cdot \text{m}^{-3} \end{cases} \tag{7}$$

Table 8 PFC simulation energy analysis of failure point C

Axial Stress $\sigma_1$ /MPa	Elastic strain energy $U^e$ /KJ·m <sup>-3</sup>	Dissipated energy $U^d$ /KJ·m <sup>-3</sup>	Friction energy $U^f$ /KJ·m <sup>-3</sup>	Input energy $U$ /KJ·m <sup>-3</sup>	$U^e/U$	$U^d/U$
0.85	214.55	88.39	29.42	302.94	0.708	0.292
0.90	235.49	79.84	25.52	315.33	0.747	0.253
0.95	261.01	75.79	23.20	336.80	0.775	0.225
1.00	284.91	20.31	4.25	305.22	0.933	0.067

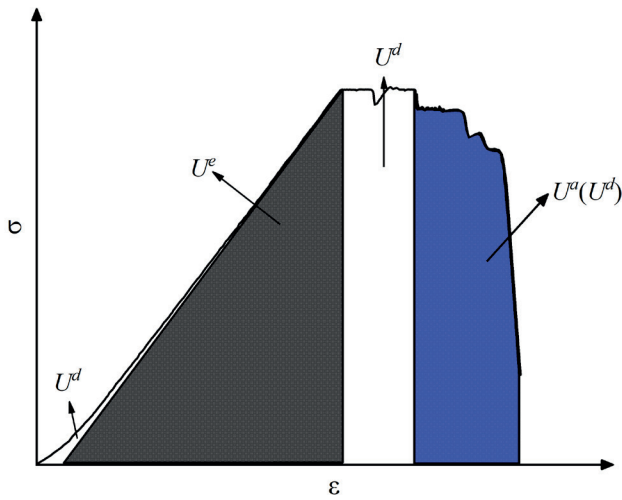


Fig. 14 Corresponding relationship between elastic strain energy and failure energy

According to the energy values obtained by PFC numerical simulation and theoretical calculation based on experiments, combined with Eq. (6) and Eq. (7), the  $A_{EF}$  values and rock burst grade evaluation are listed in Table 9 under different axial stress ( $\sigma_1$ ).

It can be seen that the  $A_{EF}$  of sandstone increases as the axial stress ( $\sigma_1$ ) increases. On the one hand, the accumulated elastic energy of the rock mass increases while the axial stress ( $\sigma_1$ ) increases. On the other hand, due to insufficient internal development of rock samples under higher axial stress ( $\sigma_1$ ), the dissipation energy transformed from the elastic strain energy decreases, resulting in the greater residual elastic energy. Therefore, the rock burst shows a trend from weakness to moderation.

In general, the prediction results of rock burst tendency are credible. However, it should be noted that the  $A_{EF}$  values of numerical simulation are much larger than theoretical calculation results under the axial stress of  $0.90 \sigma_p$  and  $0.95 \sigma_p$ , indicating that the numerical simulation method is more safer in rock burst warning.

### 5 Conclusions

Based on PFC simulation, the PSC model is introduced and further optimized to investigate the internal microscopic damage mechanism under uniaxial compression time-dependent deformation failure test. The research results of PFC simulation and experiments are as follows:

Table 9 Calculation results of residual elastic energy index and rock burst grade evaluation

Axial Stress $\sigma_1$ /MPa	$A_{EF}/(\text{kJ}\cdot\text{m}^{-3})$		Rock burst grade evaluation
	PFC simulation	Experiment	
$0.85 \sigma_p$	54.46	51.88	weak rock burst
$0.90 \sigma_p$	69.59	52.89	weak rock burst
$0.95 \sigma_p$	91.80	71.56	weak rock burst
$1.00 \sigma_p$	160.27	154.48	moderate rock burst

1. The stress-strain curves simulated by the optimized PSC model are consistent with experiments basically. The time-dependent deformation stage (BC stage) can be divided into three parts: the initial strain stage, the steady-state strain stage and the accelerated strain stage. As the axial stress increases, the strain amount of BC stage decreases and the specimen enters the accelerated strain stage rapidly.
2. The variation law of the number of micro-cracks with time is similar with the law of axial strain during the BC stage. The less micro-cracks generated at failure point C while the axial stress ( $\sigma_1$ ) increases, because the development of micro-cracks is insufficient under higher axial stress ( $\sigma_1$ ), the tensile cracks are always dominant during the whole failure process.
3. Based on the energy conversion of analysis, it is found that sandstone performs energy accumulation before the failure point C. As the axial stress ( $\sigma_1$ ) increases, the absorbed  $U^e$  increases and the required  $U^d$  decreases when the rock sample fails. After the point C,  $U^e$  has a small increase because the strain rate changes faster than the failure relaxation rate.
4. The  $A_{EF}$  of sandstone increases as the axial stress increases ( $\sigma_1$ ), and the rock burst shows a tendency that from weakness to moderation. In addition, the  $A_{EF}$  values predicted by PFC numerical simulation is larger than experiments, which is more safer for rock burst prediction.

### Acknowledgement

This work was supported by the National Natural Science Foundation of China (No. U2034203), the Natural Science Foundation of Hubei Province of China (No. 2020CFA049), Hubei Key Laboratory of Disaster Prevention and Mitigation (China Three Gorges University) open fund project (No.2020KJZ07).

## References

- [1] Yang, X.-J., Guo, Z.-B. "Mine geological engineering", China University of Mining and Technology Press, 2018. ISBN 9787564626686 (in Chinese)
- [2] Yang, Y.-S., Zhou, H., Zhang, C.-Q., Zhang, K., Yan, F. "Experimental investigation on time-lag failure properties of marble under uniaxial compressive test", *Rock and Soil Mechanics*, 32(9), pp. 2714–2720, 2011. (in Chinese)  
<https://doi.org/10.3969/j.issn.1000-7598.2011.09.026>
- [3] Xu, L.-S., Wang, L.-S. "Research on rockburst character and prevention measure of Erlang Mountain highway tunnel", *China Journal of Highway and Transport*, 16(1), pp. 74–76, 2003. (in Chinese)  
<https://doi.org/10.1007/BF02911033>
- [4] Liu, N., Zhang, C.-S., Wu, X.-M., Chu, W.-J. "Time-dependent failure of deep-buried marble in Jinping II Hydropower Station", *Advances in Science and Technology of Water Resources*, 33(2), pp. 63–67, 2013. (in Chinese)
- [5] Cui, Z., Hou, J., Wu, X.-M., Chu, W.-J. "Influence of time-dependent of crack propagation of brittle on long-term stability of Jinping water diversion tunnel", *Chinese Journal of Rock Mechanics and Engineering*, 33(5), pp. 984–885, 2014. (in Chinese)  
<https://doi.org/10.13722/j.cnki.jrme.2014.05.014>
- [6] Chen, B.-R., Feng, X.-T., Ming, H.-J., Zhou, H., Zeng, X.-H., Feng, G.-L., Xiao, Y.-X. "Evolution law and mechanism of rockburst in deep tunnel: time delayed rockburst", *Chinese Journal of Rock Mechanics and Engineering*, 31(3), pp. 561–569, 2012. (in Chinese)
- [7] Liu, N., Zhang, C.-S., Chu, W.-J. "Simulation time-dependent failure of deep marble with particle flow code", *Chinese Journal of Rock Mechanics and Engineering*, 30(10), pp. 1989–1997, 2011. (in Chinese)  
<https://doi.org/10.1016/j.cnsns.2011.01.018>
- [8] Sun, J.-S., Chen, M., Jiang, Q.-H. "Numerical simulation of meso-mechanical characteristics of creep damage evolution for Jinping marble", *Rock and Soil Mechanics*, 34(12), pp. 3601–3608, 2013. (in Chinese)  
<https://doi.org/10.16285/j.rsm.2013.12.016>
- [9] Jiang, Q., Li, J., Luo, Z., Xu, X., Assefa, E., Deng, H. "Study on the time-lag failure of sandstone with different degrees of unloading damage", *Periodica Polytechnica Civil Engineering*, 63(1), pp. 206–214, 2019.  
<https://doi.org/10.3311/PPci.13260>
- [10] Zhang, W.-D., Ma, T.-H., Tang, C.-A., Tang, L.-X. "Research in characteristics of rockburst and rules of microseismic monitoring at diversion tunnels in Jinping II hydropower station", *Chinese Journal of Rock Mechanics and Engineering*, 33(2), pp. 339–348, 2014. (in Chinese)  
<https://doi.org/10.13722/j.cnki.jrme.2014.02.017>
- [11] Xie, H.-P., Ju, Y., Li, L.-Y. "Energy mechanism of deformation and failure of rock masses", *Chinese Journal of Rock Mechanics and Engineering*, 27(9), pp. 1729–1740, 2008. (in Chinese)
- [12] Liu, W., Zhang, S., Sun, B. "Energy evolution of rock under different stress paths and establishment of a statistical damage model", *KSCE Journal of Civil Engineering*, 23, pp. 4274–4286, 2019.  
<https://doi.org/10.1007/s12205-019-0590-4>
- [13] Zhang, Y., Shao, Z., Wei, W., Qiao, R. "PFC simulation of crack evolution and energy conversion during basalt failure process", *Journal of Geophysics and Engineering*, 16(3), pp. 639–651, 2019.  
<https://doi.org/10.1093/jge/gxz036>
- [14] Liu, W.-R., Yin, Z.-Q., Yuan, A.-Y., Li, C.-M. "Particle-discrete-element-method-based research on acoustic emission characteristics and energy evolution laws of surrounding rock in different lithologic roadway", *Journal of Mining & Safety Engineering*, 34(2), pp. 363–370, 2017. (in Chinese)  
<https://doi.org/10.13545/j.cnki.jmse.2017.02.024>
- [15] Wu, S., Yang, X.-C., Guo L.-J. "Thinking and prospect of overall planning for deep metal mine in high stress environment", *Journal of China Coal Society*, 44(5), pp. 1432–1436, 2019. (in Chinese)  
<https://doi.org/10.13225/j.cnki.jccs.2019.6023>
- [16] Deng, H.-F., Zhi, Y.-Y., Duan, L.-L., Pan, D., Li, J.-L. "Mechanical properties of sandstone and damage evolution of microstructure under water-rock interaction", *Rock and Soil Mechanics*, 40(9), pp. 3447–3456, 2011. (in Chinese)  
<https://doi.org/10.16285/j.rsm.2018.1002>
- [17] Ulusay, R. "Laboratory Testing: ISRM Suggested Method for the Determination of Mode II Fracture Toughness", In: *The ISRM suggested methods for rock characterization, testing and monitoring: 2007-2014*, Springer, 2014, pp. 47–48. ISBN 978-3-319-07712-3  
<https://doi.org/10.1007/978-3-319-07713-0>
- [18] Potyondy, D. O., Cundall, P. A. "A bonded-particle model for rock", *International Journal of Rock Mechanics and Mining Sciences*, 41(8), pp. 1329–1364, 2004.  
<https://doi.org/10.1016/j.ijrmms.2004.09.011>
- [19] Lee, H., Jeon, S. "An experimental and numerical study of fracture coalescence in pre-cracked specimens under uniaxial compression", *International Journal of Solids and Structures*, 48(6), pp. 979–999, 2011.  
<https://doi.org/10.1016/j.ijsolstr.2010.12.001>
- [20] Meng, J.-J., Cao, P., Zhang, K., Tan, P. "Brazil split test of flattened disk and rock tensile strength using particle flow code", *Journal of Central South University (Science and Technology)*, 44(6), pp. 2449–2454, 2013. (in Chinese)
- [21] Xu, J.-M., Xie, Z.-L., Jia, H.-T. "Simulation of mesomechanical properties of limestone using particle flow code", *Rock and Soil Mechanics*, 31(Suppl 2), pp. 390–395, 2010. (in Chinese)  
<https://doi.org/10.16285/j.rsm.2010.s2.039>
- [22] Yin, X.-T., Zheng, Y.-N., Ma, S.-K. "Study of inner scale ratio of rock and soil material based on numerical tests of particle flow code", *Rock and Soil Mechanics*, 32, pp. 1211–1215, 2011. (in Chinese)  
<https://doi.org/10.16285/j.rsm.2011.04.017>
- [23] Zhao, Y., Wang, Y., Wang, W., Wan, W., Tang, J. "Modeling of nonlinear rheological behavior of hard rock using triaxial rheological experiment", *International Journal of Rock Mechanics and Mining Sciences*, 93, pp. 66–75, 2017.  
<https://doi.org/10.1016/j.ijrmms.2017.01.004>
- [24] Li, S.-Y. He, T.-M, Yin, X.-C. "Rock fracture mechanics", Science Press, 2019. ISBN 9787030443991 (in Chinese)
- [25] Potyondy, D. O. "Simulating stress corrosion with a bonded-particle model for rock", *International Journal of Rock Mechanics and Mining Sciences*, 44(5), pp. 677–691, 2007.  
<https://doi.org/10.1016/j.ijrmms.2006.10.002>

- [26] Manouchehrian, A., Cai, M. "Influence of material heterogeneity on failure intensity in unstable rock failure", *Computer and Geotechnics*, 71, pp. 237–246, 2016.  
<https://doi.org/10.1016/j.compgeo.2015.10.004>
- [27] Wu, Z., Fan, L., Liu, Q., Ma, G. "Micro-mechanical modeling of the macro-mechanical response and fracture behavior of rock using the numerical manifold method", *Engineering Geology*, 225, pp. 49–60, 2017.  
<https://doi.org/10.1016/j.enggeo.2016.08.018>
- [28] Zhang, S., Ma, T., Tang, C., Jia, P., Wang, Y. "Microseismic monitoring and experimental study on mechanism of delayed rockburst in deep-buried tunnels", *Rock Mechanics and Rock Engineering*, 53, pp. 2771–2788, 2020.  
<https://doi.org/10.1007/s00603-020-02069-4>
- [29] Xie, H.-P., Ju, Y., Li, L.-Y. "Criteria for strength and structural failure of rocks based on energy dissipation and energy release principles", *Chinese Journal of Rock Mechanics and Engineering*, 24 (17), pp. 3003–3010, 2005. (in Chinese)  
<https://doi.org/10.3321/j.issn:1000-6915.2005.17.001>
- [30] Wang, Z.-L., Hao, S.-Y., Zheng, J., Tian, N.-C., Zha, F.-S., Shi, H. "Study on energy properties and failure behaviors of heat-treated granite under static and dynamic compression", *Mechanics of Advanced Materials and Structures*, 27(6), pp. 462–472, 2019.  
<https://doi.org/10.1080/15376494.2018.1479808>
- [31] Gong, F.-Q., Yan, J.-Y., Li, X.-B. "A new criterion of rock burst proneness based on the linear energy storage law and the residual elastic energy index", *Chinese Journal of Rock Mechanics and Engineering*, 37(9), pp. 1993–2014, 2018. (in Chinese)  
<https://doi.org/10.13722/j.cnki.jrme.2018.0232>